

ReSem3D: Refinable 3D Spatial Constraints via Fine-Grained Semantic Grounding for Generalizable Robotic Manipulation

Chenyu Su, Weiwei Shang, Chen Qian, Fei Zhang, and Shuang Cong

Code: github.com/scy-v/ReSem3D Homepage: ReSem3D.github.io

Abstract—Semantics-driven 3D spatial constraints align high-level semantic representations with low-level action spaces, facilitating the unification of task understanding and execution in robotic manipulation. The synergistic reasoning of Multimodal Large Language Models (MLLMs) and Vision Foundation Models (VFMs) enables cross-modal 3D spatial constraint construction. Nevertheless, existing methods have three key limitations: (1) coarse semantic granularity in constraint modeling, (2) lack of real-time closed-loop planning, (3) compromised robustness in semantically diverse environments. To address these challenges, we propose ReSem3D, a unified manipulation framework for semantically diverse environments, leveraging the synergy between VFMs and MLLMs to achieve fine-grained visual grounding and dynamically constructs hierarchical 3D spatial constraints for real-time manipulation. Specifically, the framework is driven by hierarchical recursive reasoning in MLLMs, which interact with VFMs to automatically construct 3D spatial constraints from natural language instructions and RGB-D observations in two stages: part-level extraction and region-level refinement. Subsequently, these constraints are encoded as real-time optimization objectives in joint space, enabling reactive behavior to dynamic disturbances. Extensive simulation and real-world experiments are conducted in semantically rich household and sparse chemical lab environments. The results demonstrate that ReSem3D performs diverse manipulation tasks under zero-shot conditions, exhibiting strong adaptability and generalization.

Index Terms—Multimodal Large Language Models, Vision Foundation Models, Task and Motion Planning, Manipulation.

I. INTRODUCTION

WITH the advancement of robotic autonomy in unstructured environments, the growing diversity of semantic descriptions and the complexity of visual modeling have become critical challenges limiting system generalization and robustness [1]. Spatial constraints [2], [3] serve as the critical interface between high-level semantic representations and low-level action spaces, enabling the mapping of abstract semantics into executable actions. Recent advances in cross-modal reasoning powered by Multimodal Large Language Models (MLLMs) [4] and Vision Foundation Models (VFMs) [5], [6] have significantly improved visual grounding capability, which is crucial for constructing accurate 3D spatial constraints. For instance, tweezers-based grasping entails localizing the coarse semantic grasp region and reasoning about the 3D geometric relationships between the tweezer tips and the grasp

point. Based on these inferred relations, spatial constraint models can be constructed and parsed in real-time by the constraint optimizer, thereby enabling closed-loop control and fine-grained manipulation in dynamic environments.

However, current methods lack an optimizable intermediate representation that effectively links linguistic intent with the action space, thereby hindering consistent alignment between semantic goals and physical execution. As a core intermediate representation, 3D spatial constraints parameterize the mapping from semantic intent to executable actions through a set of task-grounded poses. Nevertheless, the geometric reasoning and spatial localization capabilities of MLLMs remain insufficient for directly deriving fine-grained constraints from language. Prior efforts have leveraged MLLMs and VFMs to enhance language–vision semantic alignment [7], [8], facilitating the construction of 3D spatial constraints for motion planning [9], [10]. These constraints often remain limited to coarse localization and lack semantic-guided refinement. Furthermore, downstream controllers typically rely on task-space planning, which is limited by the stability and efficiency of inverse kinematics solvers. These limitations raise two critical challenges: 1) how to design a flexible and optimizable 3D spatial constraint model that automatically maps semantic intent to robotic actions, and 2) how to ensure stable closed-loop and real-time execution within the low-level action space in semantically diverse environments.

To overcome the first challenge, we propose a two-stage hierarchical 3D spatial constraint modeling approach driven by the synergistic reasoning of VFMs and MLLMs: part-level constraint extraction and region-level constraint refinement. The part-level extraction leverages VFMs to identify semantically relevant part-level regions from the RGB observation, while generating explicit digital markers as visual prompts to facilitate MLLMs in coarse-grained constraint extraction. The region-level refinement builds dense semantic grids within masked regions, enabling fine-grained semantic grounding of geometric features by MLLMs. Subsequently, 3D spatial constraints are encoded as cost functions parsed in real-time, and supplied to downstream optimizers. To tackle the second challenge, inspired by a finite-horizon optimal control approach grounded in a general-purpose physics simulator [11], [12], we implement a real-time Model Predictive Path Integral (MPPI) control algorithm in the Isaac Gym platform [13], which delivers 15 Hz joint-space velocity commands instead of task-space commands for stable closed-loop execution.

In addition, we develop a Task and Motion Planning (TAMP) framework that extends the hierarchical recursive

The authors are with the Department of Automation, University of Science and Technology of China, Hefei 230027, China (e-mail: suchenyu@mail.ustc.edu.cn; wwshang@ustc.edu.cn; qian_chen@ustc.edu.cn; zfei@ustc.edu.cn; scong@ustc.edu.cn). Corresponding author: Weiwei Shang.

prompting structure of Liang et al. [14], driven by MLLM-based reasoning, enabling autonomous and closed-loop manipulation from perception to action. The framework demonstrates semantics-driven adaptability by autonomously determining the required granularity of 3D spatial constraints from natural language instructions. It decomposes multi-stage tasks and generates precondition checks, postcondition evaluations, and optimizable cost functions necessary for the operation of each subtask. Building on this, a subtask-level backtracking strategy is formulated, leveraging precondition feasibility to initiate cross-stage replan, enabling behavior recovery and reactive control under dynamic perturbations.

The contributions of this work are summarized as follows:

- 1) We propose a two-stage hierarchical constraint modeling framework that integrates VFMs and MLLMs to build semantically adaptive, multi-granularity 3D spatial constraints, effectively bridging the gap between high-level semantics and low-level actions.
- 2) Closed-loop control for complex long-horizon tasks with fine-grained semantic grounding is achieved for the first time with the newly developed MLLM-driven TAMP framework, which performs autonomous multi-stage task decomposition with condition reasoning and cost optimization.
- 3) Through extensive simulations and real-world experiments in semantically rich household and sparse chemical lab environments, we successfully validate Re-Sem3D’s robust zero-shot capabilities, demonstrating strong generalization and reactive property.

The remainder of this paper is organized as follows: In Section II, we review related works including foundation models and robotic manipulation. In Section III, we present the proposed system architecture in detail. In Section IV we demonstrate the performance of our method in semantically diverse environments, chemical and household, through simulation and real-world experiments. In Section V, we discuss the advantage, limitations and future work. Finally, we conclude this work in Section VI.

II. RELATED WORKS

A. Visual Grounding with Foundation Models

Visual grounding refers to mapping semantic features from natural language to image regions and spatial entities, evolving from low-level perception to semantic spatial reasoning with the advancement of foundation models. Prior VFMs focused on robust image perception, leveraging self-supervised learning [15], [16] and architectures including CNNs [17], [18] and Vision Transformers [19], which produce visual encodings for downstream tasks like object detection [20], [21], segmentation [22], [23], and feature extraction [24]. Furthermore, pixel-level parsing was enhanced through latent feature encoding and embedded visual prompts [25], [26]. Subsequently, Vision-Language Models (VLMs) perform multimodal semantic grounding through visual-linguistic representations, achieving notable progress in image-text retrieval [27] and open-vocabulary object detection [28], but still struggle with fine-grained visual grounding. Building on this, researchers

introduced Large Language Models (LLMs) [29] into vision-language systems, leading to MLLMs [30] that incorporate visual features as context for multimodal reasoning. Despite this, MLLMs remain dependent on front-end visual encoders, limiting spatial precision and semantic understanding. Recent studies have explored the synergy between VFMs and MLLMs by embedding visual prompts for semantic alignment [7], but fine-grained visual grounding remains a critical limitation. To address this challenge, we propose a multi-granularity semantic understanding framework with hierarchical multimodal reasoning, featuring part-level extraction and region-level refinement to enable fine-grained visual grounding.

B. Spatial Constraints in Robotic Manipulation

Spatial constraints are essential for robotic manipulation, bridging high-level semantics and low-level actions to ensure task feasibility. Conventional methods construct constraints through explicit geometric modeling of object shapes, contact dynamics, and environmental structure [31], [32] to enable motion planning. While physically interpretable and effective in structured scenarios, their dependence on accurate modeling constrains their flexibility in complex settings. Recently, perception-driven learning has been used to infer potential manipulation regions from visual observations, including affordance recognition [33], grasp pose detection [34], [35], target pose estimation [36], and semantic keypoint generation [37]. These approaches have further extended to multimodal manipulation frameworks that incorporate foundation model reasoning [38], [39]. While capable of adapting to object deformations and semantic changes, they still require manual data collection and struggle with fine-grained semantic parsing and precise modeling of complex geometric relationships. Current approaches integrate language and vision models to enable zero-shot semantic region perception [2], [9]. Nevertheless, aforementioned methods typically lack fine-grained semantic localization and executable geometric specifications. To overcome these limitations, we propose a two-stage 3D spatial constraint modeling framework that hierarchically maps natural language instructions to semantic objectives, enabling fine-grained and executable spatial constraints.

C. Task and Motion Planning

Task and Motion Planning (TAMP) provides a pivotal framework connecting high-level task reasoning with low-level motion execution. Conventional approaches often leverage formal languages such as PDDL and HTN to model symbolic tasks, solving task sequences and motion trajectories through logic-geometric and mixed-integer programming [40], [41]. Although offering strong interpretability, these methods rely on manually designed task models and action primitives, limiting their adaptability in open environments. With the advancement of LLMs, recent works have explored zero-shot task planning based on predefined motion primitives [42]. However, these approaches lack effective modeling of geometric constraints and environmental dynamics. Building on these developments, recent research has explored integrating LLMs with motion planning to enable high-level task decomposition

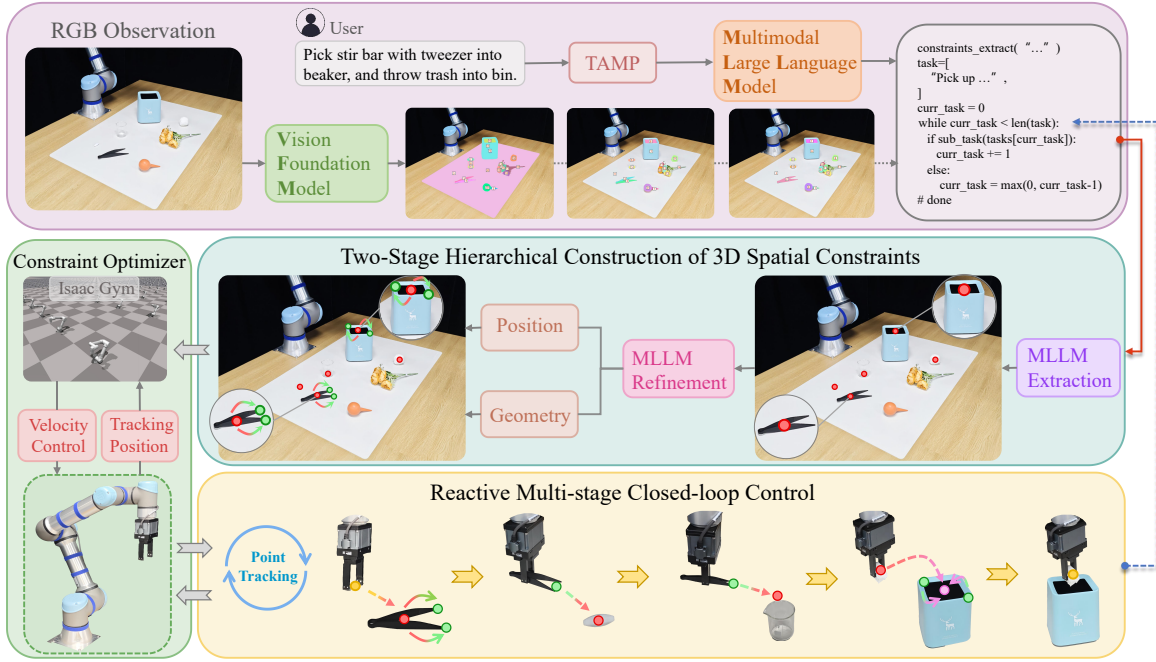


Fig. 1. Overall Framework. Given natural language instruction and RGB-D observations, VFM segments semantically relevant part-level regions and overlays visual prompts to facilitate initial constraint generation. Under the MLLM-driven TAMP framework, constraint modeling is conducted hierarchically in two stages: part-level extraction and region-level refinement. The resulting 3D spatial constraints are encoded as cost function for real-time parsing and solved in closed-loop by MPPI-based optimizer in Isaac Gym, enabling joint-space velocity control with point tracking.

and continuous action generation without predefined primitives [10]. Although such methods enhance the flexibility of TAMP, they often depend on online optimization in task space, posing challenges for real-time execution. In order to address these challenges, we employ a real-time MPPI optimizer built on Isaac Gym, leveraging joint velocity control to enhance reactive behavior during execution. Concurrently, subtask-level constraints and optimization objectives are automatically generated by the MLLM, enabling effective closed-loop control and zero-shot adaptation in dynamic environments.

III. METHOD

In this section, we first formulate ReSem3D as a real-time constrained optimization problem to standardize task objectives and constraint. Subsequently, we propose a two-stage hierarchical spatial constraint model with semantic adaptivity for multi-granularity 3D reasoning. Thereafter, we derive a real-time closed-loop control strategy for solving the optimization problem. Finally, we integrate MLLM-driven reasoning to automate TAMP, enabling end-to-end closed-loop execution.

A. ReSem3D Problem Formulation

As shown in Fig. 1, given a free-form natural language instruction $\mathcal{L} = \{L_1, L_2, \dots, L_n\}$ from the user, \mathcal{L} typically exhibits significant long-term dependencies and complex semantic reasoning. Directly generating complete 3D spatial constraints and optimizing them both compromises reasoning accuracy and complicates constraint modeling. Therefore, ReSem3D employs a hierarchical modeling strategy by decomposing the task into sequential subtasks and performing

constraint reasoning and optimization progressively for each $L_i, i \in \{1, 2, \dots, n\}$.

Specifically, for the i -th subtask instruction L_i , the instantiation of the 3D spatial constraint model is defined as

$$f : (L_i, O_i) \rightarrow \mathcal{C}_i^{\text{init}} \quad (1)$$

where O_i denotes the RGB-D sensor observations, $\mathcal{C}_i^{\text{init}} \in SE(3)$ denotes the initial set of spatial constraints mapped by f . In order to capture uncertainties in dynamic environments, we introduce external dynamic evolution and disturbances \mathcal{E}_i . Additionally, we define $\mathbf{T}_e(t) \in SE(3)$ as the end-effector pose at time t , and S as the known kinematic and physical model. At each stage i , ReSem3D addresses task execution by resolving the constrained optimization problem in real-time:

$$\begin{aligned} & \underset{\mathbf{v}(t)}{\text{argmin}} \quad \mathcal{J}(\mathbf{T}_e(t), \mathcal{C}_i) \\ & \text{subject to} \quad \mathcal{C}_i^{\text{init}} = f(L_i, O_i), \\ & \quad \mathcal{C}_i = g(\mathcal{C}_i^{\text{init}}, \mathcal{E}_i), \\ & \quad \epsilon_{\text{pre}}(\mathbf{T}_e(t), \mathcal{C}_i) \leq \epsilon_{\text{pre}}, \\ & \quad \epsilon_{\text{post}}(\mathbf{T}_e(t), \mathcal{C}_i) \leq \epsilon_{\text{post}}, \\ & \quad \mathbf{v}(t), \mathbf{T}_e(t) \in \text{Feasible}(S) \end{aligned} \quad (2)$$

where $\mathcal{J}(\mathbf{T}_e(t), \mathcal{C}_i)$ is the real-time optimized cost function, $g(\cdot)$ denotes the instantiation mapping that updates spatial constraints based on external disturbances, $\epsilon_{\text{pre}}(\mathbf{T}_e(t), \mathcal{C}_i)$ and $\epsilon_{\text{post}}(\mathbf{T}_e(t), \mathcal{C}_i)$ represent the precondition and postcondition constraints for subtask execution, with ϵ_{pre} and ϵ_{post} specifying their tolerance thresholds. The set $\text{Feasible}(S)$ enforces consistency with the robot kinematic and physical model,

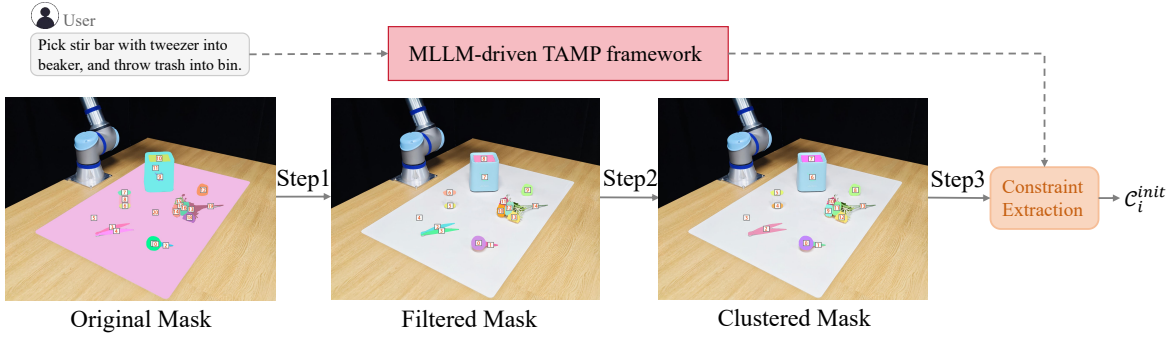


Fig. 2. Part-Level Constraint Extraction: Original mask is generated via Fast Segment Anything (FastSAM), followed by mask filtering, part-level semantic consistency cluster, and centroid annotation to extract part-level spatial constraints within the MLLM-driven TAMP framework.

$v(t) \in \mathbb{R}^n$ is the joint space velocity, serving as the decision variable, with n denoting the degrees of freedom.

Given the previously described configurations, ReSem3D decomposes long-horizon manipulation tasks into multi-stage real-time constrained optimization problems, enabling closed-loop dynamic control for each sub-task. Subsequently, the processed decision variable $v(t)$ directly serves as the joint velocity command, enabling the robot to perform tasks effectively in dynamic environments.

B. Two-Stage Hierarchical 3D Spatial Constraint Model

To instantiate the mapping $f : (L_i, O_i) \rightarrow C_i^{\text{init}}$, we leverage VFM to prompt the MLLM for fine-grained visual grounding, enabling the automated construction of a two-stage hierarchical 3D spatial constraint model comprising part-level constraint extraction and region-level constraint refinement.

1) *Part-Level Constraint Extraction*: As illustrated in Fig. 2, given subtask instruction L_i and RGB-D observation $O_i \in \mathbb{R}^{H \times W \times 4}$, we apply the pretrained image segmentation model [5] to produce the initial set of masks $M = \{m_1, m_2, \dots, m_g\}$, where $m_j \in \{0, 1\}^{H \times W}$ and $\forall j \in \{1, \dots, g\}$. Here, H and W denote the height and width of the image, respectively. To extract high-quality and discriminative part-level constraints, we design the following three-step post-processing strategy.

Step 1: Mask Filtering. A dual-filtering pipeline is applied to promote valid and distinguishable masks, resulting in the refined mask set M_{filtered} .

a) *Area-based Filtering*: we retain masks within the valid area range and define the mask set as

$$M_{\text{area}} = \{m_j \in M \mid \alpha \cdot A_{\text{img}} \leq \text{Area}(m_j) \leq \beta \cdot A_{\text{img}}\} \quad (3)$$

where A_{img} denotes the image area, α and β are thresholds.

b) *Structural Independence Filtering*: we omit any mask that contains more than a specified number of other valid masks, and define the subset M_{contain} as

$$M_{\text{contain}} = \{m_j \in M \mid N_{\text{sub}}(m_j) < 3\} \quad (4)$$

in which $N_{\text{sub}}(m_j)$ denotes the count of masks contained within mask m_j , defined as

$$N_{\text{sub}}(m_j) = |\{m_k \in M \mid m_k \subset m_j\}| \quad (5)$$

Finally, The resulting effective mask set after the dual-filtering step is defined as

$$M_{\text{filtered}} = M_{\text{area}} \cap M_{\text{contain}} \quad (6)$$

Step 2: Part-Level Semantic Consistency Clustering. Density-based clustering (DBSCAN) [43] is performed on the filtered mask set to further reduce visual ambiguity and redundancy, with masks of identical semantic labels merged within each cluster. The clustered mask set is denoted as

$$M_{\text{cluster}} = \text{DBSCAN}(M_{\text{filtered}}) \quad (7)$$

where $M_{\text{cluster}} = \{\tilde{m}_1, \tilde{m}_2, \dots, \tilde{m}_e\}$, and e is the number of clustered masks. To further extract effective part-level constraints, we define the centroid coordinate c_j for each clustered mask $\tilde{m}_j \in M_{\text{cluster}}$ as

$$c_j = \frac{1}{|\tilde{m}_j|} \sum_{(x,y) \in \tilde{m}_j} \begin{bmatrix} x \\ y \end{bmatrix} \quad (8)$$

where (x, y) denotes the 2D coordinates of the pixels in the mask \tilde{m}_j , and $|\tilde{m}_j|$ is the number of pixels in \tilde{m}_j .

Step 3: Part-Level Constraint Extraction. Each centroid in the coordinate set $C = \{c_1, c_2, \dots, c_q\}$ is sequentially assigned a numeric label from the label set $\mathcal{Z} = \{0, 1, \dots, q-1\}$ to enhance visual grounding of MLLM. These labels are overlaid onto the original RGB image $I_{\text{rgb}} \in \mathbb{R}^{H \times W \times 3}$ to form an explicit visual prompt. Together with the subtask instruction L_i , the resulting multimodal input is fed into the MLLM, which leverages semantic grounding to extract the labels relevant to the instruction. Finally, the extracted labels are projected into 3D space via the depth information $I_{\text{depth}} \in \mathbb{R}^{H \times W}$, completing the localization of initial constraint C_i^{init} .

2) *Region-Level Constraint Refinement*: As shown in Fig. 3, to enhance the granularity and adaptability of spatial constraints, we propose a semantic-adaptive region-level refinement method that automatically extracts semantic information and selects between two refinement strategies: geometric constraint refinement and positional constraint refinement. The former focuses on fine-grained structural priors within the mask region, while the latter emphasizes the spatial layout of the semantically mapped area.

Geometric Constraint Refinement: Given the mask \tilde{m}_j associated with the extracted centroid coordinate $c_j \in C$ by

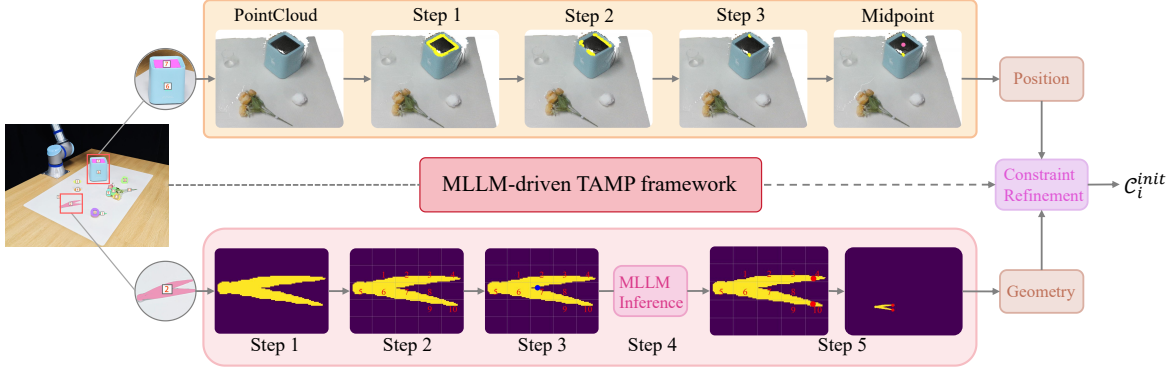


Fig. 3. Region-Level Constraint Refinement. Within the MLLM-driven TAMP framework, this module encompasses two strategies: geometric and positional constraint refinement. The geometric refinement adjusts the tweezers’ grasp point from the center to the two tips, thereby introducing detailed geometric priors. The positional refinement localizes the trash bin’s placement to the midpoint between symmetrical centers, thereby enhancing the spatial precision.

the MLLM, the geometric constraint refinement is applied to enhance fine-grained visual grounding and proceeds through the following five steps.

Step 1: Mask Normalization. Proportional discrepancies among different masks \tilde{m}_j are mitigated by cropping the effective region of each mask and uniformly scaling them, thereby embedding all masks consistently onto the fixed-resolution standard canvas. Specifically, we first extract coordinates of the foreground pixels in \tilde{m}_j as

$$\mathcal{S}_j = \{(x, y) \mid \tilde{m}_j(x, y) = 1\} \quad (9)$$

where \mathcal{S}_j denotes the set of foreground pixel coordinates. Subsequently, we determine the effective region of \tilde{m}_j by computing the boundary parameters of \mathcal{S}_j as

$$\begin{aligned} t_j &= \min_{(x,y) \in \mathcal{S}_j} y, & b_j &= \max_{(x,y) \in \mathcal{S}_j} y \\ l_j &= \min_{(x,y) \in \mathcal{S}_j} x, & r_j &= \max_{(x,y) \in \mathcal{S}_j} x \end{aligned} \quad (10)$$

here t_j , b_j , l_j and r_j denote the top, bottom, left, and right boundaries, respectively. The mask \tilde{m}_j is then cropped according to these boundaries and resized to a fixed resolution $H_r \times W_r$. The cropped mask $\tilde{m}_j^c = \tilde{m}_j(t_j : b_j, l_j : r_j)$ has dimensions $W_c = r_j - l_j + 1$ in width and $H_c = b_j - t_j + 1$ in height, where the scaling factors are defined as

$$\alpha_x = \frac{W_r}{W_c}, \quad \alpha_y = \frac{H_r}{H_c} \quad (11)$$

in which α_x and α_y denote the scaling factors in the horizontal and vertical directions, respectively. Subsequently, we apply nearest-neighbor interpolation to resize the mask to the target dimensions as

$$\tilde{m}_j^r = \mathcal{R}(\tilde{m}_j^c, \alpha_x, \alpha_y) \quad (12)$$

where \mathcal{R} denotes nearest-neighbor interpolation, and \tilde{m}_j^r is the resized mask. To maintain clear mask boundaries and prevent excessive fitting to image edges, the resizing resolution is usually smaller than the target canvas resolution. Consequently, the resized mask is further aligned onto the standardized canvas. Given the target resolution of $H_t \times W_t$, the target mask \tilde{m}_j^t is defined as

$$\tilde{m}_j^t = \tilde{m}_j^r(y - \Delta_y, x - \Delta_x) \quad (13)$$

where $\Delta_x = W_t - W_r/2$ and $\Delta_y = H_t - H_r/2$ denote the horizontal and vertical offsets, respectively, which ensure the mask remains centered within the image.

Step 2: Grid Construction and Label Embedding. In order to improve visual grounding of geometric structures, grid construction and label embedding are performed on the target mask image. Specifically, the j -th mask \tilde{m}_j^t is divided into $G_h \times G_w$ grids, where the width w_c and height h_c of each grid are determined by the target resolution $H_t \times W_t$ as follows:

$$w_c = \frac{W_t}{G_w}, \quad h_c = \frac{H_t}{G_h} \quad (14)$$

For the arbitrary grid at the k -th row and s -th column, where $k \in \{0, \dots, G_h - 1\}$, $s \in \{0, \dots, G_w - 1\}$, the coordinate region covered by the grid is expressed as

$$\mathcal{G}_{k,s}^j = \left\{ (x, y) \mid \begin{array}{l} k \cdot h_c \leq y < (k+1) \cdot h_c, \\ s \cdot w_c \leq x < (s+1) \cdot w_c \end{array} \right\} \quad (15)$$

The foreground density $\rho_{k,s}^j$ for each $\mathcal{G}_{k,s}^j$ is determined by

$$\rho_{k,s}^j = \frac{\mathcal{P}_{k,s}^j}{w_c \cdot h_c} \quad (16)$$

where $\mathcal{P}_{k,s}^j = \sum_{(x,y) \in \mathcal{G}_{k,s}^j} [\tilde{m}_j^t(x, y) = 1]$ denotes the set of foreground pixels within $\mathcal{G}_{k,s}^j$, and $|\mathcal{P}_{k,s}^j|$ is the number of pixels. When the foreground density $\rho_{k,s}^j$ surpasses the assignment threshold τ , the semantic label $\ell_{k,s}^j \in \{0, 1, \dots, N_{valid} - 1\}$ is assigned to the grid. We define the mapping $\mathcal{U} : \mathcal{G}_{k,s}^j \rightarrow \ell_{k,s}^j$ to associate each grid with the semantic label, where N_{valid} indicates the total number of grids satisfying the threshold condition. The centroid within the grid are then calculated as

$$\mathbf{c}_j^{k,s} = \frac{1}{|\mathcal{P}_{k,s}^j|} \sum_{(x,y) \in \mathcal{P}_{k,s}^j} \begin{bmatrix} x \\ y \end{bmatrix} \quad (17)$$

Step 3: Centroid mapping and label association. The centroid coordinates $\mathbf{c}_j \in C$ extracted from the part-level constraints are mapped onto the target mask and associated with the grid semantic labels $\ell_{k,s}^j$, which are overlaid on the target mask as textual prompts to enhance the fine-grained

geometric understanding of MLLM. Subsequently, we map the centroid $\mathbf{c}_j = \begin{bmatrix} x_j \\ y_j \end{bmatrix}$ into the target mask as follows:

$$\bar{x}_j = \frac{x_j - l_j}{\alpha_x} + \Delta_x, \quad \bar{y}_j = \frac{y_j - t_j}{\alpha_y} + \Delta_y \quad (18)$$

where $\bar{\mathbf{c}}_j = \begin{bmatrix} \bar{x}_j \\ \bar{y}_j \end{bmatrix}$ denotes the coordinate in the target mask. To establish the correspondence with grid labels, $\bar{\mathbf{c}}_j$ is assigned to its corresponding grid $\mathcal{G}_{k,s}^j$ by Equation (15), and then projected to the grid centroid $\mathbf{c}_j^{k,s}$ following Equation (17), thereby associating it to the semantic label $\ell_{k,s}^j$.

Step 4: Fine-grained semantic reasoning by MLLM. Achieving region-level constraint refinement and deriving new labels $\hat{\ell}_{k,s}^j$ based on the target geometric involve feeding the original RGB image I_{rgb} , the original mask \tilde{m}_j , and the target mask \tilde{m}_j as visual prompts into the MLLM. Subsequently, the numerical label z_j and the semantic label $\ell_{k,s}^j$ are presented as textual prompts to the MLLM for reasoning.

Step 5: Region-Level Constraint Extraction. The refined constraint is constructed by inversely mapping the labels $\hat{\ell}_{k,s}^j$ to their corresponding grids $\mathcal{G}_{k,s}^j$ via the instantiated mapping $\mathcal{U} : \mathcal{G}_{k,s}^j \rightarrow \ell_{k,s}^j$. The associated grid centroids $\mathbf{c}_j^{k,s}$ are then projected to the original mask coordinate as \mathbf{c}_j using Equations (17) and (18). Finally, the 2D coordinates are transformed into 3D space under the depth information $I_{\text{depth}} \in \mathbb{R}^{H \times W}$, thereby forming the initial constraint $\mathcal{C}_i^{\text{init}}$.

Positional Constraint Refinement: To address positional discrepancies in semantic grounding of objects characterized by distinct boundary features, including open-top structures, we propose a three-step refinement method that exploits edge points and spatial geometry. By integrating density peak estimation with symmetry analysis, this approach effectively mitigates MLLM limitations in position modeling, enhancing the practical feasibility of semantic grounding.

Step 1: Extraction of 3D Coordinates Along Mask Edges. The edge point set \mathcal{M}_j associated with mask \tilde{m}_j^t is defined for extracting edge points of the object as follows:

$$\mathcal{M}_j = \{(x, y) \mid \tilde{m}_j^t(x, y) = 1\} \quad (19)$$

subject to:

$$\exists(xt, yt) \in \mathcal{N}_4(x, y) \quad \text{s.t.} \quad \tilde{m}_j^t(xt, yt) = 0$$

where $\mathcal{N}_4(x, y)$ denotes the 4-neighborhood of pixel coordinate (x, y) , defined as

$$\mathcal{N}_4(x, y) = \{(x \pm 1, y), (x, y \pm 1)\} \quad (20)$$

Subsequently, with the depth information $I_{\text{depth}} \in \mathbb{R}^{H \times W}$, the set of 3D edge points \mathcal{P}_j is mapped derived as follows:

$$\mathcal{P}_j = \{\mathcal{F}_{3D}(x, y, I_{\text{depth}}) \mid \forall(x, y) \in \mathcal{M}_j\} \quad (21)$$

Step 2: Density Peak Estimation and Maximum Height Filtering. Kernel Density Estimation (KDE) is employed to model the z -axis distribution of edge points, thereby facilitating the elimination of outliers and extraction of prominent edge features. Given the set $\{z_i\}_{i=1}^N$, which represents the

heights of N edge points obtained from the mask denoted by \tilde{m}_j^t , the probability density function is approximated by

$$\hat{f}(z) = \frac{1}{Nh} \sum_{i=1}^N K\left(\frac{z - z_i}{h}\right) \quad (22)$$

where $K(\cdot)$ denotes the Gaussian kernel function and h is the bandwidth. The density peak is defined as $z^* = \arg \max_z \hat{f}(z)$. All points within the height range $|z_i - z^*| \leq \delta$ are retained, resulting in filtered 3D and 2D point sets $\mathcal{P}_j^{\text{KDE}} \subset \mathcal{P}_j$ and $\mathcal{M}_j^{\text{KDE}} \subset \mathcal{M}_j$, respectively. Subsequently, the maximum height along the z -axis in $\mathcal{P}_j^{\text{KDE}}$ is identified as z_{max} . Finally, points with heights satisfying $z_i \geq z_{\text{max}} - \eta$ are further selected, yielding the final refined point sets $\mathcal{P}_j^{\text{peak}} \subset \mathcal{P}_j^{\text{KDE}}$ and $\mathcal{M}_j^{\text{peak}} \subset \mathcal{M}_j^{\text{KDE}}$.

Step 3: Extraction of centrally symmetric point pairs. Further integration of object position and structural information is achieved by identifying centrally symmetric point pairs in 2D space, which are used to derive the refined 3D spatial constraints, denoted as $\mathcal{C}_i^{\text{init}}$. Given the centroid \mathbf{c}_j , we enumerate all point pairs $\mathbf{u}_a, \mathbf{u}_b \in \mathcal{M}_j^{\text{peak}}$ and identify the pair for which the midpoint is closest to \mathbf{c}_j , which is defined as

$$(\mathbf{u}_a^*, \mathbf{u}_b^*) = \arg \min_{\mathbf{u}_a, \mathbf{u}_b \in \mathcal{M}_j^{\text{peak}}} \left\| \frac{\mathbf{u}_a + \mathbf{u}_b}{2} - \mathbf{c}_j \right\|_2 \quad (23)$$

where $(\mathbf{u}_a^*, \mathbf{u}_b^*)$ denotes the filtered point pair, with 3D coordinates $\mathbf{p}_a, \mathbf{p}_b \in \mathcal{P}_j^{\text{peak}}$. Finally, the refined 3D spatial constraint $\mathcal{C}_i^{\text{init}}$ is expressed as

$$\mathcal{C}_i^{\text{init}} = \frac{1}{2} (\mathbf{p}_a + \mathbf{p}_b) \quad (24)$$

C. Real-Time Close-Loop Control Strategy

To solve the constrained optimization problem in Equation (2) with real-time performance, the Model Predictive Path Integral (MPPI) control algorithm is employed on the Isaac Gym simulation platform. MPPI is a stochastic optimization method designed for robot control in dynamic and uncertain environments. Essentially, the algorithm samples multiple candidate control sequences from the control input space, evaluates the cost functions based on simulated state trajectories, and updates the control policy through importance-weighted averaging. The GPU-accelerated parallel simulation enabled by Isaac Gym significantly enhances sampling efficiency, thereby supporting real-time execution in dynamic environments. For a detailed explanation of MPPI, please refer to [44], [45]. In this work, we derive the specific formulation for solving the constrained optimization problem presented in Equation (2).

To begin with, the current joint state of the robot is denoted as $\mathbf{x}(t) = \begin{bmatrix} \boldsymbol{\theta} \\ \dot{\boldsymbol{\theta}} \end{bmatrix} \in \mathbb{R}^{2n}$, comprising joint positions and velocities. With the velocity control input $\mathbf{v}(t) \in \mathbb{R}^n$, where n represents the degrees of freedom, the nonlinear state transition function can be formulated as

$$\mathbf{x}(t+1) = S(\mathbf{x}(t), \mathbf{v}(t)), \quad \mathbf{v}(t) \sim \mathcal{N}(\boldsymbol{\mu}(t), \boldsymbol{\Sigma}) \quad (25)$$

where $\mathcal{N}(\cdot)$ denotes Gaussian sampling, $\boldsymbol{\mu}(t)$ is the sampling mean, $\boldsymbol{\Sigma}$ is the covariance matrix, and S represents

the forward kinematics and physical model. At each time step, MPPI samples K distinct control sequences $\{\mathbf{V}_k\}_{k=1}^K$, where each sequence consists of velocity inputs over a time horizon T , expressed as $\mathbf{V}_k = [\mathbf{v}_k(0), \mathbf{v}_k(1), \dots, \mathbf{v}_k(T-1)]^\top$. Subsequently, each state trajectory is derived by combining the initial state $\mathbf{x}(0)$ with the forward model as

$$\mathcal{X}_k = [\mathbf{x}_k(0), \mathbf{x}_k(1), \dots, \mathbf{x}_k(T)]^\top \quad (26)$$

where $\mathbf{x}_k(t+1) = S(\mathbf{x}_k(t), \mathbf{v}_k(t))$. To further solve the problem, we introduce the forward kinematics mapping $\varphi: \mathbb{R}^{2n} \rightarrow SE(3)$, which maps the joint space state to the end-effector pose, expressed as $\mathbf{T}_e^k(t) = \varphi(\mathbf{x}_k(t))$. At this point, $\mathbf{T}_e^k(t) \in SE(3)$ denotes the end-effector pose of the k -th trajectory at time t . For each trajectory \mathcal{X}_k , the total cost is the cumulative sum of the objective function $\mathcal{J}(\cdot)$ over each time step, defined as

$$C_k = \sum_{t=0}^{T-1} \mathcal{J}(\mathbf{T}_e^k(t), \mathcal{C}_i) \quad (27)$$

For convenience in the analysis, we define the position and orientation errors as follows:

$$\mathcal{D}_p = d_p(P(\mathbf{T}_e^k(t)), P(\mathcal{C}_i)) \quad (28)$$

$$\mathcal{D}_r = d_r(R(\mathbf{T}_e^k(t)), R(\mathcal{C}_i)) \quad (29)$$

where $P(\cdot)$ and $R(\cdot)$ denote the position and quaternion components extracted from the spatial pose. The errors are calculated as $d_p(\mathbf{p}_1, \mathbf{p}_2) = \|\mathbf{p}_1 - \mathbf{p}_2\|_2$ and $d_r(\mathbf{q}_1, \mathbf{q}_2) = 2 \arccos(\max(-1, \min(1, \langle \mathbf{q}_1, \mathbf{q}_2 \rangle)))$. Subsequently, the objective function is defined as

$$\mathcal{J}(\mathbf{T}_e^k(t), \mathcal{C}_i) = \lambda_p \cdot \mathcal{D}_p + \lambda_r \cdot \mathcal{D}_r + \lambda_c \cdot \mathcal{D}_c \quad (30)$$

where λ_p and λ_r are the weights for position and orientation costs, λ_c denote the weight for the collision cost \mathcal{D}_c , which is formulated based on the ESDF representation, as described in [9]. In this work, the objective function is subject to preconditions and postconditions as specified in Equation (2), the precondition typically ensures that the end-effector is within the designated region prior to the execution stage, while the postcondition assesses whether the end-effector has successfully reached the desired pose, defined as

$$\epsilon_{\text{pre}}(\mathbf{T}_e^k(t), \mathcal{C}_i) = \mathcal{D}_p(k, t, i) \quad (31)$$

$$\epsilon_{\text{post}}(\mathbf{T}_e^k(t), \mathcal{C}_i) = \mathcal{D}_p(k, t, i) + \mathcal{D}_r(k, t, i) \quad (32)$$

After evaluating the total cost C_k , MPPI assigns weights to each sampled trajectory as follows:

$$\omega_k = \frac{1}{\eta} \exp\left(-\frac{1}{\beta}(C_k - \rho)\right), \quad \sum_{k=1}^K \omega_k = 1 \quad (33)$$

where β is the temperature parameter governing the variance of sample weights, and $\rho = \min_k C_k$ is the stability offset. The approximate optimal control sequence $\mathbf{U}^* = [\mathbf{u}_0^*, \mathbf{u}_1^*, \dots, \mathbf{u}_{T-1}^*]$ is expressed as

$$\mathbf{U}^* = \sum_{k=1}^K \omega_k \cdot \mathbf{V}_k \quad (34)$$

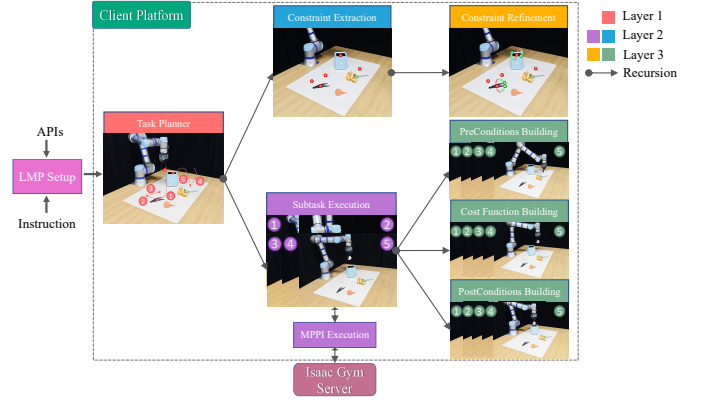


Fig. 4. MLLM-driven automated modeling and communication framework for TAMP.

Finally, the first control input \mathbf{u}_0^* of the sequence \mathbf{U}^* is applied as the velocity command to the system, and the optimization procedure is conducted iteratively.

D. MLLM-driven Automated Modeling of TAMP

As depicted in Fig. 4, the Language Model Program (LMP) framework is built on a hierarchical recursive architecture [14], enabling structured invocation and multi-level prompt nesting. Based on the framework, we have designed and encapsulated seven LMP modules within ReSem3D, corresponding respectively to Task Planner, Constraint Extraction, Constraint Refinement, Subtask Execution, Preconditions Building, Cost Function Building, and PostConditions Building. Each module implements an independent prompt structure and interfaces with system components through standardized APIs, enabling the automated modeling for task and motion planning.

During the LMP Setup phase, dependency relationships among LMP layers are established and mappings to API interfaces are configured driven by the natural language instructions. Subsequently, Task Planner performs global scheduling and intent parsing, collaborating with Constraint Extraction and Subtask Execution to model spatial constraints and execute tasks. Finally, considering the reliance on semantic understanding in spatial constraint modeling, Constraint Refinement is introduced to implement two-stage modeling with recursive parameter updates fed back to Task Planner.

Within the Subtask Execution phase, each task is decomposed into a sequence of constrained action execution units. Specifically, initiation conditions, optimization objectives, and termination criteria for action execution are formulated respectively by Preconditions Building, Cost Function Building, and Postconditions Building. Subsequently, each action execution unit activates the MPPI Execution, establishing the communication loop between the client and the Isaac Gym server. The client transmits real-time joint states and perception-fused cost functions, while the server performs GPU-accelerated MPPI sampling and optimization to synthesize continuous joint-space velocity commands, which are transmitted back to the client, thereby enabling stepwise closed-loop control.

In the course of task execution, preconditions and postconditions are monitored. Upon violation of the precondition, the

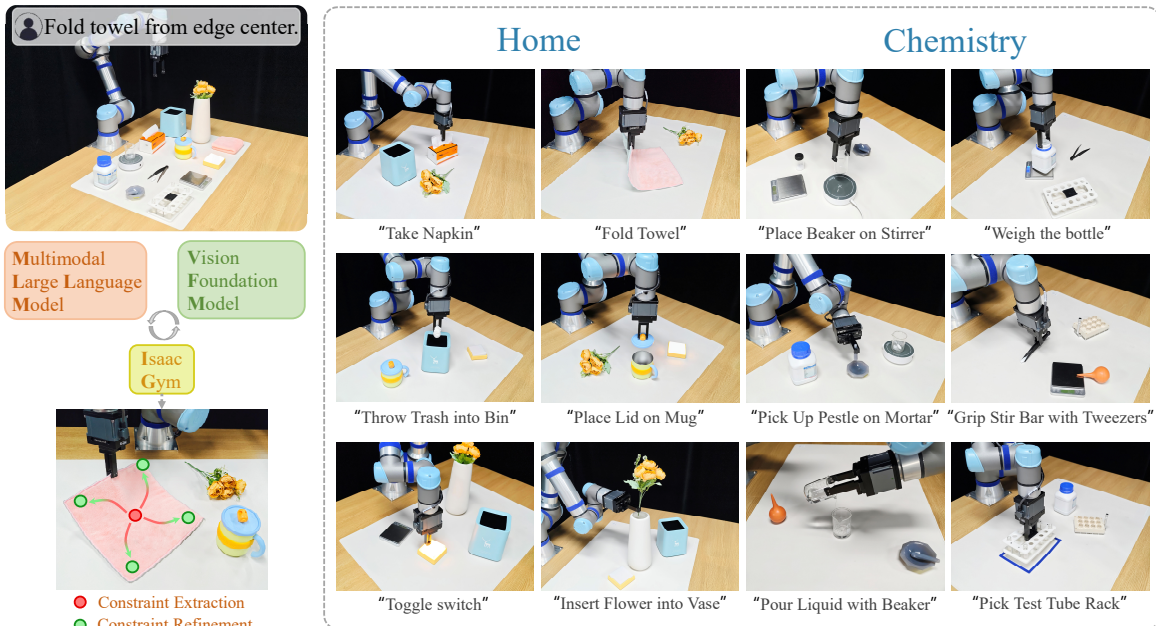


Fig. 5. ReSem3D is a unified robotic manipulation framework for semantically diverse environments. It leverages the synergy between MLLMs and VFMs to construct semantics-driven, two-stage hierarchical 3D spatial constraints, which are mapped into real-time optimization objectives in joint space to enable closed-loop perception-action control.

system backtracks and restarts the previous subtask, whereas satisfaction of the postcondition triggers progression to the next subtask. Ultimately, ReSem3D establishes a closed-loop TAMP framework centered on semantic understanding, guided by hierarchical recursion, and grounded in constraint feedback.

IV. EXPERIMENT

In this section, we first detail the experimental setup. Subsequently, we evaluate the cross-platform generalization of ReSem3D in simulated environments. Then, we demonstrate the manipulation generalization in the semantically diverse real-world environments. Furthermore, we analyze the core mechanisms of ReSem3D, exhibiting the superiority to baseline methods. Finally, we identify the key factors contributing to execution failures.

A. Experimental Setup

Hardware Configuration. As shown in Fig. 6, our real-world experimental platform is constructed around the 6-DOF Universal Robots UR5e collaborative robotic arm, equipped with a PGI-140-80 two-finger parallel gripper and an Intel RealSense D435i RGB-D camera. For simulation, we employ the Omnigibson [46] platform developed by Stanford University, and utilize both the UR5e and the 7-DOF Franka Emika Panda collaborative arms.

Tasks and Metrics. As shown in Fig. 5, we designed 12 real-world tasks (6 chemical lab scenarios and 6 household scenarios) to evaluate generalization and stability under static conditions and dynamic disturbances. In simulation, we perform 10 tasks (6 chemical lab scenarios and 4 household scenarios) to evaluate generalization across different robotic platforms under static conditions. Furthermore, we designed

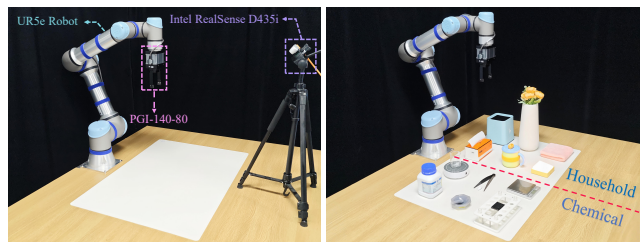


Fig. 6. Hardware Platform Configuration.

three simulated and four real-world experiments to assess the effectiveness in visual grounding. All tasks were evaluated over 10 trials, and success rate was reported.

Baselines. We compare against three representative frameworks: VoxPoser [10], ReKep [9] and CoPa [2]. VoxPoser integrates large language and vision models to generate 3D value maps interpretable by robots, enabling closed-loop trajectory synthesis without predefined motion primitives. It leverages GPT-4 and a visual frontend for semantic grounding of task objects, supporting flexible manipulation across diverse tasks. ReKep fuses VLMs and MLLMs to infer semantic keypoint constraints for structured tasks and solves end-effector trajectories in real time via hierarchical optimization. CoPa leverages foundation vision-language models to propose a two-stage task execution process, performing task-oriented grasping via coarse-to-fine visual grounding in the first stage, and identifying task-relevant spatial and geometric constraints for robot planning in the second stage. All three frameworks deeply integrate large language and vision models, employing semantics-driven visual grounding and control optimization to achieve efficient and robust robotic manipulation.

VFM and MLLM. We utilize GPT-4o [4] from OpenAI as

TABLE I
SUCCESS RATES ACROSS STATIC TASKS IN SIMULATION

Household Scenario		Success Rate		
Task	Robot Platform	Voxposer	ReKep	ReSem3D (Ours)
Toggle switch	UR5e	0/10	3/10	9/10
Fold Towel	Franka Panda	0/10	3/10	5/10
Take Napkin	Franka Panda	8/10	6/10	7/10
Cut Cake with Knife	Franka Panda	0/10	5/10	7/10
Total		20.0%	42.5%	70.0%
Chemical Lab Scenario				
Pour reagent into dish	UR5e	7/10	0/10	8/10
Weigh the Reagent Bottle	UR5e	8/10	1/10	8/10
Pick Up Pestle on Mortar	UR5e	0/10	3/10	6/10
Place Reagent Bottle on Stirrer	UR5e	7/10	2/10	8/10
Place Funnel on Iron Ring	Franka Panda	0/10	0/10	4/10
Grip Stir Bar with Tweezers	Franka Panda	0/10	0/10	5/10
Total		36.6%	10.0%	65.0%

TABLE II
VISUAL GROUNDING SUCCESS RATES IN SIMULATION

Task	Scale	ReKep	ReSem3D (Ours)
Insert Flower into Vase	150%	3/10	7/10
	70%	1/10	6/10
	40%	0/10	4/10
Insert Bread into Toaster	150%	4/10	7/10
	70%	0/10	9/10
	40%	0/10	9/10
Pick Up Pestle on Mortar	150%	8/10	8/10
	70%	7/10	9/10
	40%	1/10	9/10

a callable MLLM and combine it with the visual foundation model FastSAM [5] to enable high-efficiency multimodal reasoning (prompt design is available at [ReSem3D.github.io](https://github.com/ReSem3D)). During the dynamic disturbance phase, we incorporate the TAPNext model from Google DeepMind [47] together with real-time RGB frame input to achieve online point tracking at approximately 20 Hz. This facilitates real-time inference of evolving spatial constraints in dynamic environments, thereby enhancing the stability and robustness of task execution.

B. Evaluation of ReSem3D in Simulated Environments

As summarized in Table I, we systematically evaluate the generalization capability of ReSem3D in simulation across different robotic platforms and semantically diverse environments, comprising 4 household and 6 chemical lab tasks under static conditions. For the Toggle Switch task, the density peak in positional constraint refinement is replaced by the maximum height to enable more direct extraction of symmetric point pairs. The results demonstrate that ReSem3D exhibits strong task adaptability and cross-platform generalization under zero-shot conditions, achieving execution success rates of 70% in household and 65% in chemical lab scenarios, respectively—consistently outperforming the baseline methods. This performance is attributed to the proposed two-stage 3D spatial constraint model. Specifically, VoxPoser achieves competent performance in tasks where the 3D center point of the object



Fig. 7. Comparison between ReKep and **ReSem3D (Ours)** in Constraint Modeling. Each method has two columns presenting RGB and point cloud visualizations, and two rows for 150% and 40% object scales. The numerical labels in purple, green, and red indicate the initial 2D constraints extracted by MLLM on the toaster, vase, and pestle, respectively, while the colorful arrows indicate the refinement of geometric and positional 3D constraints.

mask spatially aligns with a feasible grasp point (e.g., napkin, reagent, and stirrer). However, the success rate drops markedly when such alignment is absent. Although ReKep consistently generates semantically meaningful keypoints across tasks, its effectiveness is limited by the mismatch between predicted and task-relevant keypoints. Notably, since depth information for transparent containers is available in Omnigibson, these objects are modeled as opaque (e.g., plastic bottles) in simulation. Despite differences from real-world visual characteristics, this scheme preserves consistency in constraint generation and manipulation strategies, ensuring rigor in evaluation.

For further analysis, we focus on the constraint modeling adopted by ReKep for open-structured containers and dual-ended semantic objects. As shown in Fig. 7, the semantic keypoints of such objects are typically extracted by the MLLM, either computing the centroid of multiple opening-edge points (e.g., the vase and toaster) or identifying functionally distinct endpoints (e.g., the narrower end of the pestle). However, constraint generation in ReKep is sensitive to keypoint spacing and considerably dependent on object scale: scale increases tend to produce redundant constraints that disrupt accurate recognition, while scale decreases often cause constraint merging, leading to the loss of semantic keypoints. By comparison,

TABLE III
SUCCESS RATES IN REAL-WORLD ENVIRONMENTS.

Task Scenarios		Voxposer		Rekep		ReSem3D (Ours)	
Household Scenario	Stage	Static	Dist.	Static	Dist.	Static	Dist.
Take Napkin	M1	3/10	2/10	5/10	4/10	7/10	5/10
Fold Towel	M1, M2	0/10	0/10	2/10	1/10	5/10	3/10
Place Lid on Mug	M1, M3	0/10	0/10	3/10	1/10	5/10	4/10
Toggle switch	M1, M3	0/10	0/10	1/10	0/10	4/10	3/10
Insert Flower into Vase	M1, M3	0/10	0/10	2/10	1/10	6/10	4/10
Throw Trash into Bin	M1, M3	7/10	6/10	6/10	5/10	8/10	7/10
Total		16.6%	13.3%	31.6%	20.0%	58.3%	43.3%
Chemical Lab Scenario							
Place Beaker on Stirrer	M1	0/10	0/10	1/10	0/10	6/10	5/10
Pour Liquid with Beaker	M1	0/10	0/10	1/10	0/10	7/10	6/10
Pick Test Tube Rack	M1	1/10	0/10	1/10	0/10	6/10	5/10
Pick Up Pestle on Mortar	M1, M2	0/10	0/10	1/10	0/10	5/10	4/10
Grip Stir Bar with Tweezers	M1, M2	0/10	0/10	0/10	0/10	4/10	2/10
Weigh the bottle	M1, M3	7/10	5/10	5/10	4/10	8/10	6/10
Total		13.3%	8.3%	15.0%	6.6%	60.0%	46.6%

TABLE IV
VISUAL GROUNDING SUCCESS RATES IN REAL WORLD

Task	CoPa	ReSem3D (Ours)
Fold Towel	0/10	6/10
Toggle Switch	1/10	5/10
Pick Up Pestle on Mortar	0/10	7/10
Grip Stir Bar with Tweezers	0/10	6/10
Total	2.5%	60%

ReSem3D demonstrates significantly greater stability under scale variation, exhibiting enhanced robustness against scale perturbations. This advantage is substantiated in Table II, where ReSem3D consistently outperforms baseline methods in visual grounding success rates on the Vase, Toaster and Pestle scaled to 150%, 70%, and 40%. These results indicate that the method effectively alleviates the impact of scale variation in open-structured container and dual-ended semantic object manipulation, thereby enhancing the zero-shot generalization.

C. Evaluation of ReSem3D in real-world Environments

In this section, we systematically evaluate the generalization of ReSem3D in real-world environments through a set of semantically diverse manipulation tasks, including 6 household and 6 chemical lab scenarios. As shown in Table III, M1, M2, and M3 indicate part-level constraint extraction, geometric constraint refinement, and positional constraint refinement, respectively. Static denotes environments without external disturbances, whereas “Dist.” refers to dynamic disturbances from manually displacing objects during task execution. Compared with baselines, ReSem3D achieves significant task execution performance, with 58.3% (Static) and 43.3% (Dist.) in the household scenario, and 60% (Static) and 45% (Dist.) in the chemical lab scenario, demonstrating superior zero-shot generalization and enhanced robustness against dynamic disturbances. A comprehensive analysis is presented below.

Specifically, household scenarios are characterized by rich semantic structures and modest constraint precision, which

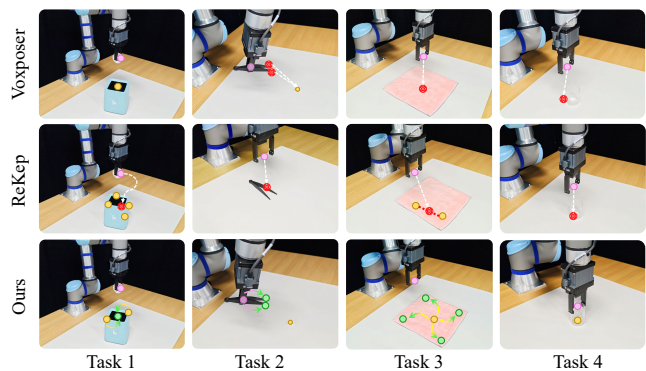


Fig. 8. Comparison between Baselines and **ReSem3D (Ours)** in Constraint Modeling and Closed-Loop Execution. Tasks 1 to 4 correspond to the execution for the bin, tweezer, towel, and beaker. The pink marks indicate end-effector positions or grasped constraints, yellow marks denote extracted constraints, green marks represent refined constraints, red marks highlight non-executable constraints, and colorful arrows show constraint refinement.

enable baselines to retain considerable generalization in constraint modeling and object localization. Voxposer is robust in tasks where the 3D center points of object masks (e.g., napkins, trash, bins) are directly graspable, consistent with its simulation performance. For other tasks, failure occurs when the localization results do not meet the grasping requirements. Additionally, Rekep effectively extracts rich semantic keypoints for MLLM interpretation. However, complex semantic structures and fine-grained constraints (e.g., locating towel corners, detecting raised switch edges) surpass its interpretative capabilities. In contrast, chemical lab scenarios are typified by sparse semantic structure and prevalence of transparent materials, which degrade depth perception and necessitate greater spatial precision. These conditions further constrain baseline generalization (e.g., localizing beaker center, identifying pestle’s narrow tip), causing a continued decline in success rates. Building on these insights, ReSem3D introduces a two-stage 3D spatial constraint model that integrates semantic understanding and spatial reasoning, achieving 1.7% (Static) and

3.3% (Dist.) improvement in task success rates, maintaining strong robustness in semantically diverse environments.

To qualitatively analyze the advantages of ReSem3D, we focus on its performance in semantic constraint modeling and closed-loop execution efficiency, as shown in Fig. 8. It can be observed that the semantic constraints from VoxPoser mainly concentrate around the coarse center of objects, lacking fine-grained geometric awareness and operability. Additionally, the absence of point clouds for transparent objects in chemical scenarios (e.g., beaker in Task 4) presents a significant challenge to accurate 3D center localization. Furthermore, the 5Hz 3D value map update rate restricts the responsiveness of closed-loop trajectory planning. Similarly, while ReKep constructs semantically directed constraints, it is limited in the accuracy (e.g., the center of the beaker, bin, and tweezer) and adjustability (e.g., the corners of the towel, the tips of the tweezer) of constraint generation. Its performance depends on the effectiveness of constraint generation and high-level reasoning by MLLM. Moreover, closed-loop optimization at 10Hz is constrained by the efficiency of inverse kinematics solving, leading to unstable real-time responsiveness.

Furthermore, we compare with CoPa, which also adopts a coarse-to-fine visual grounding framework. As shown in Table IV, we evaluate four representative tasks from Table III to examine whether the visual localization is sufficient for successful task execution. Experimental results show that ReSem3D achieves a 60% success rate, significantly outperforming CoPa. A detailed qualitative analysis in Fig. 9 shows that, while CoPa performs hierarchical grounding, its fine-grained localization precision is limited to the part level, making it insufficient for tasks requiring finer spatial reasoning.

V. DISCUSSION

Given challenges to achieve fine-grained visual grounding and maintaining real-time closed-loop control, ReSem3D achieves better performance via three strategies: (1) **Refinable Two-Stage 3D Spatial Constraint Model**. Semantics-driven 3D spatial constraints are generated in two stages, enabling automatic refinement and adaptation in semantically rich and sparse environments. (2) **Real-Time Closed-Loop Optimization in Joint Space**. Semantics-driven 3D spatial constraints are formulated as joint-space cost functions and optimized using a real-time constrained solver running over 15 Hz, enabling reactive closed-loop control in dynamic environments. (3) **MLLM-driven Automated TAMP Modeling**. ReSem3D autonomously determines the suitable granularity for 3D spatial constraint modeling from natural language instructions and generates cost functions for the real-time constrained optimizer. Additionally, it decomposes multi-stage tasks and generates preconditions and postconditions, enabling temporal management and dynamic backtracking during execution.

Ultimately, the stable operation of ReSem3D requires effective coordination across functional modules. To systematically identify failure causes, we conduct independent validation for each sub-module by calculating the failure rate based on Table III. Specifically, since the VFM module lacks semantic guidance, it may fail to provide task-relevant semantic grounding in 7% of cases, thereby generating irrelevant candidates.



Fig. 9. Comparison between Copa and **ReSem3D (Ours)** in visual grounding.

Reasoning failures in constraint extraction and refinement, constituting 16% and 28% of failures respectively, arise from insufficient cross-modal semantic grounding and limited spatial reasoning. The Constrained Optimization module often suffers from slow convergence under significant pose variation in 11% of occurrences, due to multi-objective complexity. The TAPNext module exhibits reduced tracking accuracy under occlusion or inaccurate point cloud mappings in 38% of situations, thereby breaking the perception-action loop.

To address these challenges, future work will explore the integration of MLLM-based self-correction strategies, global optimization algorithms, and multi-view fusion methods to further enhance the robustness and adaptability of the framework.

VI. CONCLUSION

In this work, we present ReSem3D, a unified robotic manipulation framework for semantically diverse environments. By integrating MLLMs and VFMs, the framework automatically constructs semantically grounded two-stage 3D spatial constraints. These are embedded into a hierarchical TAMP model and formulated as joint-space cost functions, enabling real-time and robust closed-loop control. The proposed approach facilitates hierarchical constraint modeling from semantically rich to sparse environments, enabling multi-stage task execution and condition-aware dynamic backtracking. Extensive simulation and real-world experiments demonstrate that ReSem3D outperforms existing baselines in zero-shot manipulation tasks across semantically diverse environments and different robotic platforms.

REFERENCES

- [1] H. R. Walke, K. Black, T. Z. Zhao, Q. Vuong, C. Zheng, P. Hansen-Estruch, A. W. He, V. Myers, M. J. Kim, M. Du *et al.*, “Bridgedata v2: A dataset for robot learning at scale,” in *Proceedings of CoRL*. PMLR, 2023, pp. 1723–1736.
- [2] H. Huang, F. Lin, Y. Hu, S. Wang, and Y. Gao, “Copa: General robotic manipulation through spatial constraints of parts with foundation models,” in *Proceedings of IROS*. IEEE, 2024, pp. 9488–9495.
- [3] F. Liu, K. Fang, P. Abbeel, and S. Levine, “Moka: Open-vocabulary robotic manipulation through mark-based visual prompting,” in *Proceedings of ICRA*, 2024.
- [4] J. Achiam, S. Adler, S. Agarwal, L. Ahmad, I. Akkaya, F. L. Aleman, D. Almeida, J. Altenschmidt, S. Altman, S. Anadkat *et al.*, “Gpt-4 technical report,” *arXiv preprint arXiv:2303.08774*, 2023.
- [5] X. Zhao, W. Ding, Y. An, Y. Du, T. Yu, M. Li, M. Tang, and J. Wang, “Fast segment anything,” *arXiv preprint arXiv:2306.12156*, 2023.
- [6] A. Kirillov, E. Mintun, N. Ravi, H. Mao, C. Rolland, L. Gustafson, T. Xiao, S. Whitehead, A. C. Berg, W.-Y. Lo *et al.*, “Segment anything,” in *Proceedings of ICCV*, 2023, pp. 4015–4026.
- [7] J. Yang, H. Zhang, F. Li, X. Zou, C. Li, and J. Gao, “Set-of-mark prompting unleashes extraordinary visual grounding in gpt-4v,” *arXiv preprint arXiv:2310.11441*, 2023.

- [8] J. Yang, R. Tan, Q. Wu, R. Zheng, B. Peng, Y. Liang, Y. Gu, M. Cai, S. Ye, J. Jang *et al.*, “Magma: A foundation model for multimodal ai agents,” in *Proceedings of CVPR*, 2025, pp. 14203–14214.
- [9] W. Huang, C. Wang, Y. Li, R. Zhang, and L. Fei-Fei, “Rekep: Spatio-temporal reasoning of relational keypoint constraints for robotic manipulation,” *arXiv preprint arXiv:2409.01652*, 2024.
- [10] W. Huang, C. Wang, R. Zhang, Y. Li, J. Wu, and L. Fei-Fei, “Voxposer: Composable 3d value maps for robotic manipulation with language models,” in *Proceedings of CoRL*. PMLR, 2023, pp. 540–562.
- [11] Y. Zhang, C. Pezzato, E. Trevisan, C. Salmi, C. H. Corbato, and J. Alonso-Mora, “Multi-modal mppi and active inference for reactive task and motion planning,” *IEEE Rob. Autom. Lett.*, 2024.
- [12] C. Pezzato, C. Salmi, E. Trevisan, M. Spahn, J. Alonso-Mora, and C. H. Corbato, “Sampling-based model predictive control leveraging parallelizable physics simulations,” *IEEE Rob. Autom. Lett.*, 2025.
- [13] V. Makoviychuk, L. Wawrzyniak, Y. Guo, M. Lu, K. Storey, M. Macklin, D. Hoeller, N. Rudin, A. Allshire, A. Handa *et al.*, “Isaac gym: High performance gpu-based physics simulation for robot learning,” *arXiv preprint arXiv:2108.10470*, 2021.
- [14] J. Liang, W. Huang, F. Xia, P. Xu, K. Hausman, B. Ichter, P. Florence, and A. Zeng, “Code as policies: Language model programs for embodied control,” in *Proceedings of ICRA*. IEEE, 2023, pp. 9493–9500.
- [15] T. Chen, S. Kornblith, M. Norouzi, and G. Hinton, “A simple framework for contrastive learning of visual representations,” in *Proceedings of ICML*. PmlR, 2020, pp. 1597–1607.
- [16] K. He, H. Fan, Y. Wu, S. Xie, and R. Girshick, “Momentum contrast for unsupervised visual representation learning,” in *Proceedings of CVPR*, 2020, pp. 9729–9738.
- [17] Y. LeCun, L. Bottou, Y. Bengio, and P. Haffner, “Gradient-based learning applied to document recognition,” *Proceedings of the IEEE*, vol. 86, no. 11, pp. 2278–2324, 2002.
- [18] A. Krizhevsky, I. Sutskever, and G. E. Hinton, “Imagenet classification with deep convolutional neural networks,” *Commun. ACM*, vol. 60, no. 6, pp. 84–90, 2017.
- [19] A. Dosovitskiy, L. Beyer, A. Kolesnikov, D. Weissenborn, X. Zhai, T. Unterthiner, M. Dehghani, M. Minderer, G. Heigold, S. Gelly *et al.*, “An image is worth 16x16 words: Transformers for image recognition at scale,” in *Proceedings of ICLR*, 2020.
- [20] R. Girshick, J. Donahue, T. Darrell, and J. Malik, “Rich feature hierarchies for accurate object detection and semantic segmentation,” in *Proceedings of CVPR*, 2014, pp. 580–587.
- [21] J. Redmon, S. Divvala, R. Girshick, and A. Farhadi, “You only look once: Unified, real-time object detection,” in *Proceedings of CVPR*, 2016, pp. 779–788.
- [22] J. Long, E. Shelhamer, and T. Darrell, “Fully convolutional networks for semantic segmentation,” in *Proceedings of CVPR*, 2015, pp. 3431–3440.
- [23] V. Badrinarayanan, A. Kendall, and R. Cipolla, “Segnet: A deep convolutional encoder-decoder architecture for image segmentation,” *IEEE Trans. Pattern Anal. Mach. Intell.*, vol. 39, no. 12, pp. 2481–2495, 2017.
- [24] H. Touvron, M. Cord, M. Douze, F. Massa, A. Sablayrolles, and H. Jégou, “Training data-efficient image transformers & distillation through attention,” in *Proceedings of ICML*. PMLR, 2021, pp. 10347–10357.
- [25] X. Chen, Z. Zhao, Y. Zhang, M. Duan, D. Qi, and H. Zhao, “Focalclick: Towards practical interactive image segmentation,” in *Proceedings of CVPR*, 2022, pp. 1300–1309.
- [26] X. Zou, J. Yang, H. Zhang, F. Li, L. Li, J. Wang, L. Wang, J. Gao, and Y. J. Lee, “Segment everything everywhere all at once,” *Proceedings of NeurIPS*, vol. 36, pp. 19769–19782, 2023.
- [27] A. Radford, J. W. Kim, C. Hallacy, A. Ramesh, G. Goh, S. Agarwal, G. Sastry, A. Askell, P. Mishkin, J. Clark *et al.*, “Learning transferable visual models from natural language supervision,” in *Proceedings of ICML*. PMLR, 2021, pp. 8748–8763.
- [28] S. Liu, Z. Zeng, T. Ren, F. Li, H. Zhang, J. Yang, Q. Jiang, C. Li, J. Yang, H. Su *et al.*, “Grounding dino: Marrying dino with grounded pre-training for open-set object detection,” in *Proceedings of ECCV*. Springer, 2024, pp. 38–55.
- [29] H. Touvron, T. Lavril, G. Izacard, X. Martinet, M.-A. Lachaux, T. Lacroix, B. Rozière, N. Goyal, E. Hambro, F. Azhar *et al.*, “Llama: Open and efficient foundation language models,” *arXiv preprint arXiv:2302.13971*, 2023.
- [30] H. Liu, C. Li, Q. Wu, and Y. J. Lee, “Visual instruction tuning,” *Proceedings of NeurIPS*, vol. 36, pp. 34892–34916, 2023.
- [31] L. P. Kaelbling and T. Lozano-Pérez, “Integrated task and motion planning in belief space,” *Int. J. Rob. Res.*, vol. 32, no. 9-10, pp. 1194–1227, 2013.
- [32] M. Kopicki, S. Zurek, R. Stolkin, T. Mörwald, and J. Wyatt, “Learning to predict how rigid objects behave under simple manipulation,” in *Proceedings of ICRA*. IEEE, 2011, pp. 5722–5729.
- [33] F.-J. Chu, R. Xu, and P. A. Vela, “Learning affordance segmentation for real-world robotic manipulation via synthetic images,” *IEEE Rob. Autom. Lett.*, vol. 4, no. 2, pp. 1140–1147, 2019.
- [34] H.-S. Fang, C. Wang, H. Fang, M. Gou, J. Liu, H. Yan, W. Liu, Y. Xie, and C. Lu, “Anygrasp: Robust and efficient grasp perception in spatial and temporal domains,” *IEEE Trans. Rob.*, vol. 39, no. 5, pp. 3929–3945, 2023.
- [35] D. Pavlichenko and S. Behnke, “Dexterous pre-grasp manipulation for human-like functional categorical grasping: Deep reinforcement learning and grasp representations,” *IEEE Trans. Autom. Sci. Eng.*, 2025.
- [36] L. Zheng, C. Wang, Y. Sun, E. Dasgupta, H. Chen, A. Leonardis, W. Zhang, and H. J. Chang, “Hs-pose: Hybrid scope feature extraction for category-level object pose estimation,” in *Proceedings of CVPR*, 2023, pp. 17163–17173.
- [37] T. Schmidt, R. Newcombe, and D. Fox, “Self-supervised visual descriptor learning for dense correspondence,” *IEEE Rob. Autom. Lett.*, vol. 2, no. 2, pp. 420–427, 2016.
- [38] C. Tang, D. Huang, W. Ge, W. Liu, and H. Zhang, “Grasppt: Leveraging semantic knowledge from a large language model for task-oriented grasping,” *IEEE Rob. Autom. Lett.*, vol. 8, no. 11, pp. 7551–7558, 2023.
- [39] Z. Li, J. Liu, Z. Li, Z. Dong, T. Teng, Y. Ou, D. Caldwell, and F. Chen, “Language-guided dexterous functional grasping by llm generated grasp functionality and synergy for humanoid manipulation,” *IEEE Trans. Autom. Sci. Eng.*, 2025.
- [40] N. T. Dantam, Z. K. Kingston, S. Chaudhuri, and L. E. Kavraki, “Incremental task and motion planning: A constraint-based approach,” in *Proceedings of RSS*, vol. 12. Ann Arbor, MI, USA, 2016, p. 00052.
- [41] C. R. Garrett, T. Lozano-Pérez, and L. P. Kaelbling, “Sampling-based methods for factored task and motion planning,” *Int. J. Rob. Res.*, vol. 37, no. 13-14, pp. 1796–1825, 2018.
- [42] I. Singh, V. Blukis, A. Mousavian, A. Goyal, D. Xu, J. Tremblay, D. Fox, J. Thomason, and A. Garg, “Progprompt: Generating situated robot task plans using large language models,” in *Proceedings of ICRA*. IEEE, 2023, pp. 11523–11530.
- [43] M. Ester, H.-P. Kriegel, J. Sander, X. Xu *et al.*, “A density-based algorithm for discovering clusters in large spatial databases with noise,” in *Proceedings of KDD*, vol. 96, no. 34, 1996, pp. 226–231.
- [44] G. Williams, A. Aldrich, and E. A. Theodorou, “Model predictive path integral control: From theory to parallel computation,” *J. Guid. Control Dyn.*, vol. 40, no. 2, pp. 344–357, 2017.
- [45] G. Williams, P. Drews, B. Goldfain, J. M. Rehg, and E. A. Theodorou, “Information-theoretic model predictive control: Theory and applications to autonomous driving,” *IEEE Trans. Rob.*, vol. 34, no. 6, pp. 1603–1622.
- [46] C. Li, R. Zhang, J. Wong, C. Gokmen, S. Srivastava, R. Martín-Martín, C. Wang, G. Levine, M. Lingelbach, J. Sun *et al.*, “Behavior-1k: A benchmark for embodied ai with 1,000 everyday activities and realistic simulation,” in *Proceedings of CoRL*. PMLR, 2023, pp. 80–93.
- [47] A. Zholus, C. Doersch, Y. Yang, S. Koppula, V. Patraucean, X. O. He, I. Rocco, M. S. Sajjadi, S. Chandar, and R. Goroshin, “Tapnext: Tracking any point (tap) as next token prediction,” *arXiv preprint arXiv:2504.05579*, 2025.